



Cite this: *Phys. Chem. Chem. Phys.*,  
2015, 17, 22235

# *In situ* studies of lithium-ion diffusion in a lithium-rich thin film cathode by scanning probe microscopy techniques†

Shan Yang, Binggong Yan, Tao Li, Jing Zhu, Li Lu and Kaiyang Zeng\*

This paper presents *in situ* characterization of lithium-ion diffusion at nano- to micro-meter scales in a Li-rich layered oxide thin film cathode under external bias by using Electrochemical Strain Microscopy (ESM) and Atomic Force Microscopy (AFM) techniques. The local variations of the diffusion coefficient are calculated and visualized from the ESM images. The results indicate that the Li-ion movement is closely correlated with the changes in the surface topography when the Li-rich cathode is subjected to an external bias. Furthermore, bias-induced Li-ion redistribution is partially reversible. Topography evolution due to Li-ion diffusion and relaxation behaviour are observed. The results from this *in situ* study provide the insight into the Li-ion diffusion mechanism in the cathode material and pave the way for studying the details of the diffusion-related phenomenon in Li-ion battery materials.

Received 6th April 2015,  
Accepted 22nd July 2015

DOI: 10.1039/c5cp01999k

www.rsc.org/pccp

## Introduction

With the development of the information storage and increasing demands for new power sources, Li-ion batteries (LIBs) have attracted more and more attention in recent years. This is due to the many advantages of the LIBs, such as high voltage, the non-memory effect, small volume, small self-discharging, light weight and so on.<sup>1,2</sup> In LIBs, cathode materials have been widely studied because of their important roles in determining the battery's electrochemical performance, reliability and cost. Up to now, the most widely studied cathode materials include layered LiCoO<sub>2</sub>, LiNiO<sub>2</sub>, LiCo<sub>1/3</sub>Ni<sub>1/3</sub>Mn<sub>1/3</sub>O<sub>2</sub>, spinel LiMn<sub>2</sub>O<sub>4</sub> as well as olivine LiFePO<sub>4</sub>. However, the specific capacities of those cathode materials are relatively low, approximately within the range of 120–180 mA h g<sup>-1</sup>.<sup>1</sup> In order to achieve high energy density for new generation energy storage systems, many alternative cathode materials have been developed and studied in recent years.<sup>3,4</sup> Among which, lithium-rich layered oxide material Li<sub>2</sub>MnO<sub>3</sub>–LiMO<sub>2</sub> (M = Ni, Co, Mn) is a promising cathode for LIBs due to its capability to safely deliver about twice the energy

density when compared with that of other commercial cathode materials.<sup>5–10</sup>

To understand the characteristics of LIB materials, various structural and electrochemical techniques have been used, such as X-ray diffraction (XRD), nuclear magnetic resonance, galvanostatic charge/discharge cycling, cyclic voltammetry, and electrochemical impedance spectroscopy. Almost all of these techniques are applied at macroscopic and device levels. On the other hand, it is necessary to understand the battery performances at different length scales in order to develop new battery materials or optimize their functionalities. However, the fundamental understanding from meso- to nano-scales has yet to be established for those materials. Scanning probe microscopy (SPM) is therefore an important and ideal characterization technique that is capable of *in situ* detection of certain or the changes in the localized properties, as well as the electrochemical phenomenon at micro- to nano-scales for LIB materials.<sup>11–13</sup>

During charge/discharge processes of LIBs, Li-ions undergo insertion/extraction processes between the anode and cathode materials. The irreversible diffusion of the Li-ions contributes to the impedance increase, capacity decay and power fading (aging) of the batteries. Hence, it is essential to understand the mechanisms of the Li-ion diffusion and the associated phenomenon in order to develop new generation battery materials as well as to increase the reliability of the LIBs. Recently, a newly developed SPM technique, Electrochemical Strain Microscopy (ESM), has emerged to study the local Li-ion diffusion and related electrochemical activities.<sup>14–19</sup> ESM allows applying the high frequency periodic bias through the conductive tip on the surface of the electrochemically active materials. This bias can induce localized volume change or surface

Department of Mechanical Engineering, National University of Singapore,  
9 Engineering Drive 1, 117576, Singapore. E-mail: mpezk@nus.edu.sg;  
Fax: +65 6779 1459; Tel: +65 6516 6627

† Electronic supplementary information (ESI) available: XRD patterns of Li<sub>1.2</sub>Co<sub>0.13</sub>Ni<sub>0.13</sub>Mn<sub>0.54</sub>O<sub>2</sub> thin film and AFM topographic images show grains with (003) orientation and well-defined hexagon-like geometry. The chemical diffusion coefficient of Li vs. potential during the charge state in Li-rich cathode film determined by PITT experiments. The AFM topographic images obtained by using the tip after BE-ESM imaging and a new tip on the same area. See DOI: 10.1039/c5cp01999k



deformation due to Li-ion diffusion, migration and redistribution within the material. The local surface deformation, which is defined as the electrochemical strain, can be detected by the high sensitive photodetector in the ESM system. This technique has been used to study the mechanisms of capacity fading in cathode materials for LIBs.<sup>20,21</sup> In order to eliminate the cross-talk of the surface morphology and enhance signal detection sensitivity, the band-excitation (BE) technique is used together with the ESM measurement. The BE technique excites and detects signal with a defined amplitude in a predefined frequency range, in which the contact resonance frequency is approximately located in the middle of the frequency range.<sup>22–24</sup> The BE-ESM data are then fitted with the simple harmonic oscillator (SHO) model. BE-ESM analysis can obtain several images, including resonance amplitude, resonance frequency and *Q*-factor. The resonance amplitude is a measure of electrochemical strain that provides information such as Li-ion concentration changes and electrochemical activity. Resonance frequency is associated with the contact stiffness of the sample surface whereas the resonance *Q*-factor is a measure of the relative energy dissipation of the tip-sample interaction.

In this work, a lithium-rich layered oxide cathode material,  $\text{Li}_{1.2}\text{Co}_{0.13}\text{Ni}_{0.13}\text{Mn}_{0.54}\text{O}_2$  or written as  $0.55\text{Li}_2\text{MnO}_3-0.45\text{LiCo}_{1/3}\text{Ni}_{1/3}\text{Mn}_{1/3}\text{O}_2$  based on the mass ratio, is studied by using the BE-ESM technique. At the same time, Atomic Force Microscopy (AFM) is used to obtain the high-resolution topographic images of the surface before and after the BE-ESM images. The Li-rich thin film cathode was deposited on a commercial Pt coated Si substrate by using the pulsed laser deposition (PLD) technique at an oxygen partial pressure of 350 mTorr. The as-deposited thin film was post-annealed at 800 °C with oxygen flow for 40 minutes. The average surface roughness (RMS) of the as-deposited Li-rich cathode film is about 60 nm from the AFM measurement. The detailed preparation, structure characterization and the macroscopic electrochemical properties have been previously reported by Yan and colleagues.<sup>25</sup> During the BE-ESM measurements, the Pt layer (on Si substrate) is grounded to ensure the circuit continuity. It should be mentioned that, during the ESM measurement, the bias-induced Li-ion movement includes two parts, *i.e.*, ion-migration driven by electrostatic potential difference and ion-diffusion driven by chemical concentration gradient.<sup>17</sup> When the cathode material is biased, both ion-diffusion and ion-migration occur simultaneously. However, after the removal of the bias, only the ion-diffusion is operated in the material.

## Experimental

### SPM measurements

In this study, the AFM and ESM measurements were performed using a commercial SPM system (MPF-3D, Asylum Research, USA) equipped with a BE controlling and data analysis software (Asylum Research/Oak Ridge National Laboratory, USA) at room temperature and under ambient conditions. All the SPM measurements were conducted using a commercial Ti/Pt coated Silicon conductive tip (AC240TM, Olympus, Japan). This probe has the resonance frequency of about 70 kHz, and a nominal spring

constant of  $2 \text{ N m}^{-1}$ . BE-ESM mapping was performed with  $3V_{\text{ac}}$  bias and a bandwidth of 20 kHz at a central frequency of 290 kHz.

### XRD measurement

The structures of the thin film and the substrate were characterized using X-ray diffraction (XRD) equipment (Model XRD-7000, Shimadzu Corporation, Kyoto, Japan) with  $\text{CuK}\alpha$  radiation ( $\lambda = 1.5418 \text{ \AA}$ ).

### PITT measurement

The PITT (potentiostatic intermittent titration technique) measurement (1400 CellTest System, Solartron Analytical, UK) was conducted to measure the diffusion coefficient of the Li-ions in the cathode material. During the measurements, a potential with a step increment of 10 mV was applied and the current was measured as a function of time until equilibrium was reached. The potential step was taken to the next level when the residual currents were less than 1% of the maximum current at the beginning of the potential step.

## Results and discussion

### Grain orientation of the Li-rich thin film cathode

The crystal structure of the film is determined by XRD analysis. For a particular allowed (*hkl*) reflection, the diffraction conditions will be satisfied for those grains that have their (*hkl*) planes parallel to the substrate.<sup>26</sup> For  $\text{Li}_{1.2}\text{Co}_{0.13}\text{Ni}_{0.13}\text{Mn}_{0.54}\text{O}_2$  powder, three principal diffraction peaks, (003), (101), and (104), are observed.<sup>25</sup> However, for  $\text{Li}_{1.2}\text{Co}_{0.13}\text{Ni}_{0.13}\text{Mn}_{0.54}\text{O}_2$  thin film, the relative intensity of the (003) plane reflection increases while the reflection of (101) and (104) cannot be found (Fig. S1(a), ESI<sup>†</sup>). For the layered structure cathode material, the (003) plane has the lowest surface energy since it has the highest atomic density, and the percentage of (003) oriented grains will increase as the film thickness decreases.<sup>26</sup> The presence of only (003) reflection for the Li-rich film cathode indicates that, within the sensitivity of the measurement, most grains are (003) oriented, *i.e.*, with the *c*-axis aligned normal to the plane of the film.<sup>26</sup> In addition, the (003) oriented grains usually have a flat surface with hexagonal facet texture; whereas (101) and (104) oriented grains usually have a platelet feature.<sup>27,28</sup> In consideration of the thin film preparation method, the parallel alignment of (003) planes is preferred in layered structure thin film deposited by the PLD technique.<sup>29,30</sup> Therefore, the grains with well-defined hexagon-like geometry [Fig. S1(b), ESI<sup>†</sup>] suggest a high degree of crystallinity with (003) orientated planes parallel to the substrate for the PLD deposited Li-rich layered oxide cathode material.

### Nanoscale mapping of the lithium diffusion coefficient

Fig. 1(a) to (d) are AFM topographic images ( $0.8 \times 0.8 \mu\text{m}^2$ ) on the surface of the  $\text{Li}_{1.2}\text{Co}_{0.13}\text{Ni}_{0.13}\text{Mn}_{0.54}\text{O}_2$  cathode thin film before and after the BE-ESM imaging with  $3V_{\text{ac}}$  bias. The surface of the film has distinct features such as grain, grain boundaries and the depressions between the grains. The thin



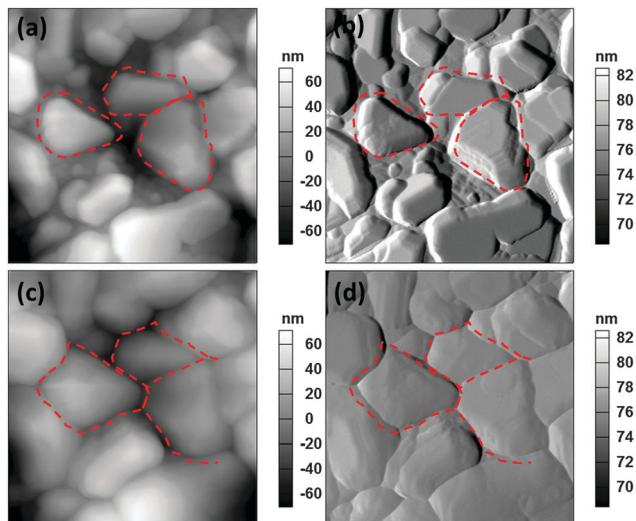


Fig. 1 (a) and (b) are the AFM height and deflection image on a  $0.8 \times 0.8 \mu\text{m}^2$  area of the sample surface in  $\text{Li}_{1.2}\text{Co}_{0.13}\text{Ni}_{0.13}\text{Mn}_{0.54}\text{O}_2$  cathode film before the BE-ESM image; (c) and (d) AFM height and deflection image after the BE-ESM imaging (with  $3V_{\text{ac}}$  bias).

film is composed of well-defined grains with grain size in the range of 50 to 200 nm. After the BE-ESM imaging, the grain topography changes significantly as indicated by the red dashed lines in Fig. 1(c) and (d), and this clearly shows the changes in the volume of the cathode material due to the bias-induced Li-ions movement and redistribution within the BE-ESM imaged area.

Fig. 2(a) to (d) are the typical BE-ESM height, amplitude, frequency and  $Q$ -factor images (after SHO fitting) of the Li-rich thin film cathode from the BE-ESM image with the  $3V_{\text{ac}}$  bias on  $100 \times 100$  grid over the  $0.8 \times 0.8 \mu\text{m}^2$  area. Fig. 2(b) shows strong variations of the contrast in the resonance amplitude over the imaged region. This indicates the different surface displacements under the external bias, which can be attributed to the different local electrochemical activity on the surface. The regions with blue colour, which show the highest amplitude values, are usually associated with the area near the depressions, or boundaries, or some small grains, indicating that these regions have largest surface displacements. The regions with yellow colour, showing the lowest amplitude value, also emerge in certain boundaries. The surface deformation changes under the bias indicate a variation of the material volume caused by a localized change in the Li-ion concentration under the electric field. Higher volume changes indicate the higher concentration of the Li-ions in that area. Generally speaking, the atoms in the grain boundary region are much more mobile than those inside the grains. In addition, depending on the structure, the boundary diffusion may be anisotropic.<sup>31</sup> Hence, the electrochemical deformation at boundaries may also be anisotropic. Fig. 2(c) and (d) show the variation of resonance frequency and  $Q$ -factor. The resonance frequency image is a measure of conservative tip–surface interaction and provides information on the contact stiffness. As shown in Fig. 2(c), the resonance frequency increases in a certain area adjacent to the grain boundaries (yellow colour) and topographical depressions. The topographical depressions

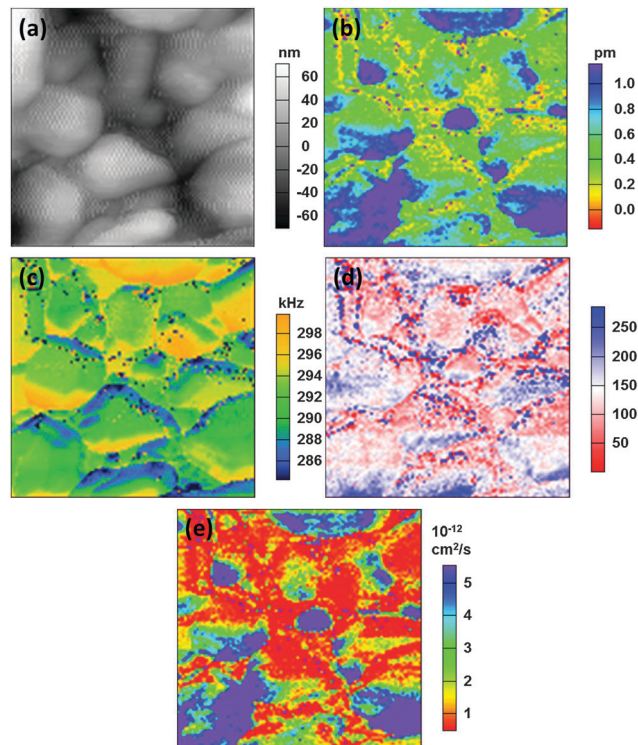


Fig. 2 (a) to (d) are the typical BE-ESM (with  $3V_{\text{ac}}$  bias) height, resonance amplitude, resonance frequency and  $Q$ -factor images, respectively; (e) is the calculated diffusion coefficient map. All the BE-ESM images are obtained with a pixel density of  $100 \times 100$  over  $0.8 \times 0.8 \mu\text{m}^2$ .

may increase the effective tip–sample contact area, hence contact stiffness is increased. The dark-spots in the figures indicate that the resonance frequency is not being tracked in those spots. The  $Q$ -factor is a measurement of the energy dissipation at the tip–surface junction. Fig. 2(d) shows that the  $Q$ -factor decreases at depressions and boundaries (red colour), indicating higher energy dissipation in these areas.

If the lithium ion transport process is diffusion-controlled and the contribution of migration is minimal, the amplitude of the surface displacement during the BE-ESM measurement in the high-frequency regime can be written as:<sup>32</sup>

$$A = 2(1 + \nu)\beta \frac{V_{\text{ac}} \sqrt{D}}{\eta \sqrt{\omega}} \quad (1)$$

where  $\nu = 0.3$  is the Poisson's ratio;  $V_{\text{ac}}$  is the AC voltage amplitude;  $\omega$  is the frequency of the applied electric field;  $D$  is the lithium diffusion coefficient;  $\eta$  describes the linear relationship between the applied field and chemical potential,<sup>32</sup> and  $\beta = 0.02349$  is the Vegard coefficient, which can be expressed as an empirical linear relationship between the lattice size and lithium concentration.<sup>14</sup> Eqn (1) shows that BE-ESM deformation is proportional to the diffusion coefficient but inversely proportional to the overpotential. If one of the two quantities is known, then the other one can be derived from the BE-ESM map. When the ESM tip was taken as a point of reference, the overpotential is equivalent to the ESM applied voltage.<sup>14</sup> Based on these assumptions, the local diffusion coefficient is first calculated from the





BE-ESM amplitude map and the corresponding spatial map is shown in Fig. 2(e). The average diffusion coefficient within the imaged region is approximately  $3 \times 10^{-12} \text{ cm}^2 \text{ s}^{-1}$ , which agrees well with the chemical diffusion coefficient of Li-ions estimated by the PITT measurements in the region of 3–4 V (Fig. S2, ESI<sup>†</sup>). This shows that BE-ESM images can be used to determine the local diffusivity as well as to obtain the corresponding local diffusion coefficients of cathode materials with certain assumptions. The diffusion map shows that the higher amplitude regions are usually associated with the higher diffusion coefficient. Hence it suggests that these higher deformation areas have higher electrochemical activities.

### Nanoscale mapping of diffusion and diffusivity loss

The local diffusivity of the Li-ions is further studied by performing multiple BE-ESM imaging (up to five times) in the same region. Fig. 3(a) to (d) are three-dimensional (3D) AFM topographic images ( $1 \times 1 \mu\text{m}^2$ ) before and after the 1st, 2nd and 5th BE-ESM imaging with  $3V_{\text{ac}}$  bias. Fig. 3(e) to (h) are the AFM topographic images ( $2 \times 2 \mu\text{m}^2$ ), in which the central  $1 \times 1 \mu\text{m}^2$  is the BE-ESM imaged area (enclosed by the square in red-colour). This is to determine the effect of the multiple BE-ESM

images and whether the effects of the applied bias are actually beyond the BE-ESM imaged area. All images are obtained from the same location with only a slight shift. Fig. 3(i) is the height profiles along the lines in Fig. 3(e) to (h). It is found that the grains expand and become attached to each other in almost all directions after the 1st BE-ESM image [Fig. 3(b)]. The grain expansion is accompanied by fill-up of the depressions between the grains. The line profile clearly shows that the peaks associated with the grains (indicated by the blue arrows) are broadened [Fig. 3(i)], indicating that the sample surface becomes more flattened after the BE-ESM imaging. On the other hand, the 3D topographic images show that the topography changes are particularly significant in the grain boundary regions, resulting in the original sharp edges of grains becoming round after the BE-ESM imaging [Fig. 3(b)]. Note that although the grains expand, they still retain their original shape and do not merge into a single larger grain after BE-ESM imaging. This suggests that the structure stability is still maintained under the external bias. Another interesting observation is that although the BE-ESM bias is only applied within the central  $1 \times 1 \mu\text{m}^2$  region, the bias actually changes the topography in the surrounding area as well [Fig. 3(f)]. The grains outside the BE-ESM imaged area

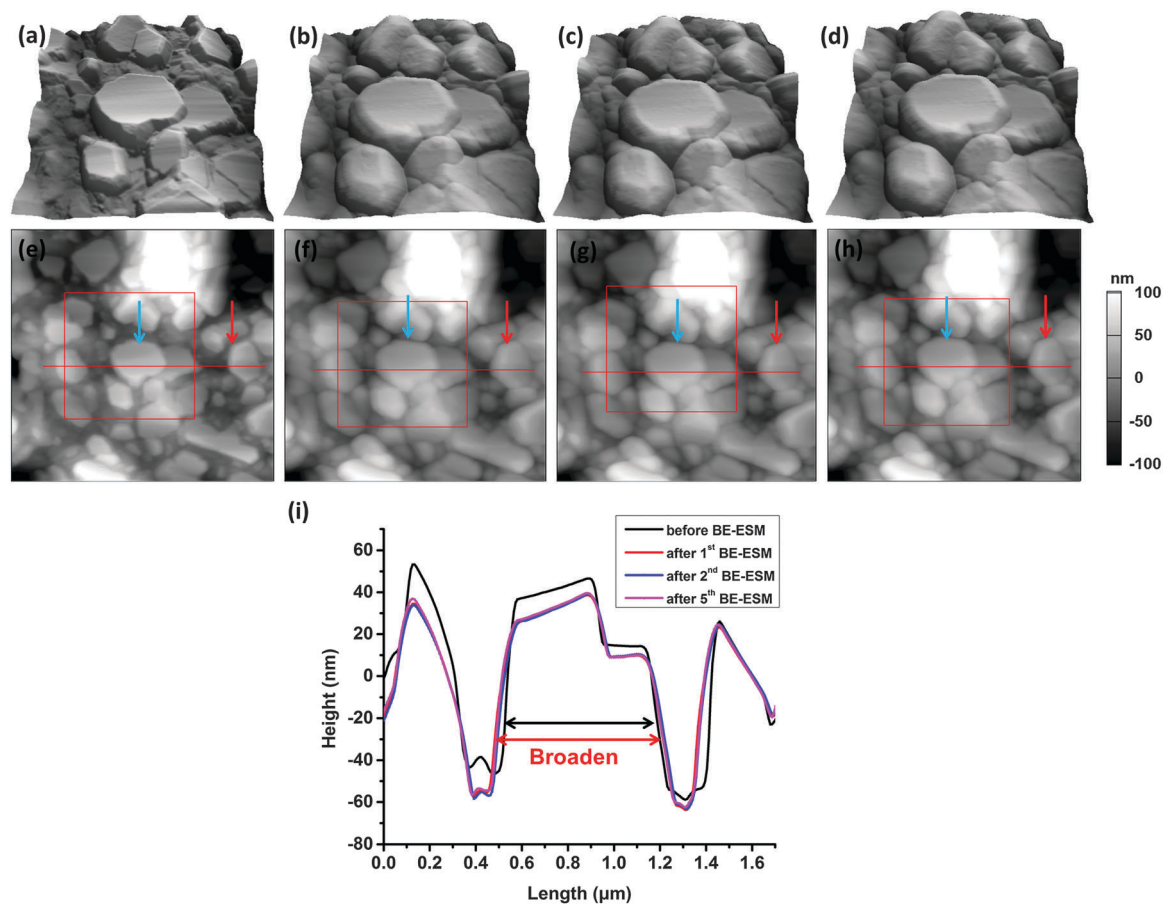


**Fig. 3** (a) to (d) are the 3D AFM height images at  $1 \times 1 \mu\text{m}^2$  area of the sample surface in  $\text{Li}_{1.2}\text{Co}_{0.13}\text{Ni}_{0.13}\text{Mn}_{0.54}\text{O}_2$  cathode film before, after 1st, 2nd and 5th BE-ESM images (with  $3V_{\text{ac}}$  bias); (e) to (h) are the corresponding AFM height images ( $2 \times 2 \mu\text{m}^2$ ), in which the BE-ESM imaged area (red square) is located approximately at the centre of the region scanned by AFM; and (i) is the height profile along the lines in the images (e) to (h), respectively. All the AFM images were scanned by a pixel density of  $256 \times 256$  and a scan rate of 1 Hz.



(for example, those indicated by the red arrows) also expand, resulting in the filling of the gaps between the individual grains. This behaviour can be related to the layered structure of the material. The Li-ions are preferred in between the layers during the redistribution under the electric field.

It should be noted that the BE technique is not operated in a normal scanning mode. During the BE measurement, the SPM tip is fixed in one location and the frequency is swept with the pre-defined range, the tip is then lifted and moved to the next location to perform the same measurement. Such measurements will be performed in a grid matrix. Hence the tip wear in the BE technique is minimal. However, to exclude the possible effects of the tip change during BE imaging, a comparative AFM scanning with the tip was performed after BE imaging and a new tip is conducted over the same region. The topography images by using old and new tips show the same features (Fig. S3, ESI<sup>†</sup>), and this indicates that the grain expansion is a real phenomenon under external electric field and not an artifact caused by the tip wearing. The topography changes are caused by the Li-ion movements and redistribution under the electric field. When the cathode is biased, both ion-diffusion and ion-migration may be operated simultaneously, while after

removing the bias, only ion-diffusion may be functioned.<sup>17</sup> Therefore, the induced Li-ion movement outside the biased area is governed by the diffusion mechanism. In a layered structure cathode, the intercalation of Li-ions into cathode can cause an extension of the *a*-axis and contraction of the *c*-axis, while the de-intercalation of Li-ions out of the cathode can cause the inverse changes in the lattice parameter.<sup>33</sup> Under the bias cycles, Li-ions diffuse in and out of the actuated grains, accompanied by volumetric expansion and reduction. The grain expansion (*a*-axis extension) indicates an increase of Li-ion concentration and Li-ions diffuse into this individual grain through a complicated boundary network. Due to the discrepant effect of oscillatory positive and negative bias, the intercalation/de-intercalation induced by the oscillatory bias cycle can be asymmetric, resulting in irreversible topography changes.

Fig. 4(a) to (c) are the 3D images of the resonance amplitude overlapped on the topographic images of the 1st, 2nd and 5th BE-ESM with the  $3V_{ac}$  bias in the same  $1 \times 1 \mu\text{m}^2$  region. In the BE-ESM measurements, the magnitude of electrochemical strain (amplitude) is proportional to the local electrochemical activity in a small volume of the material below the biased tip.<sup>18</sup> The variations in the surface deformation can be caused by a

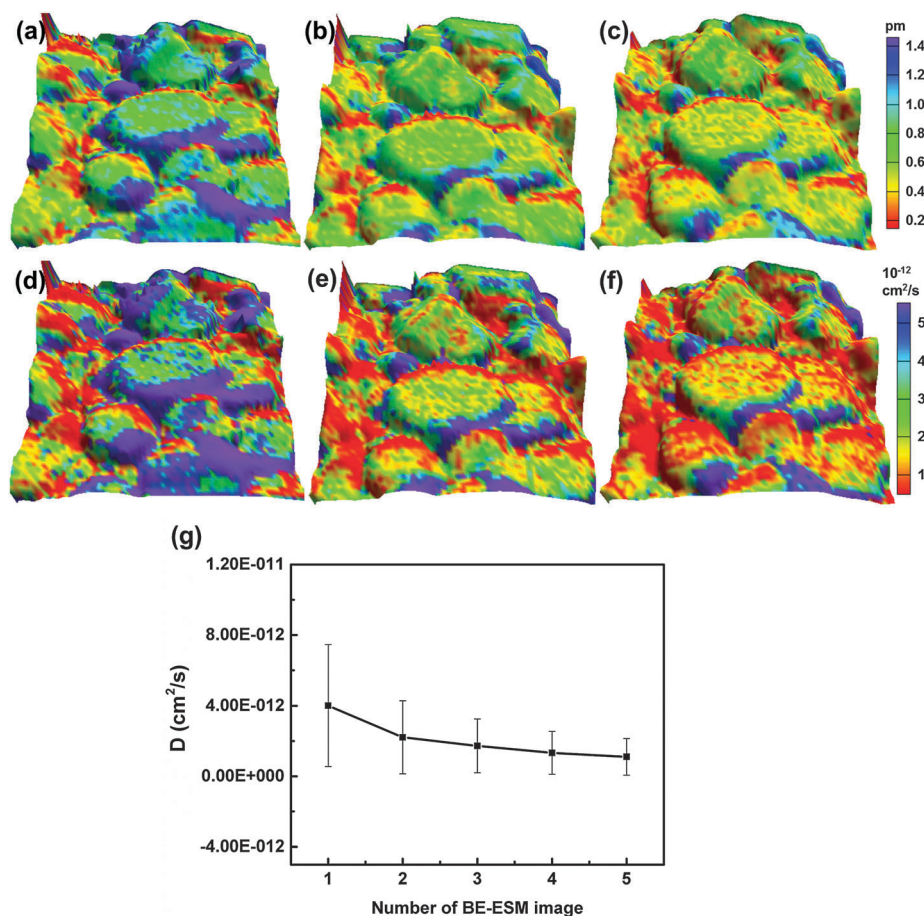


Fig. 4 BE-ESM images overlaid on topographic images (with  $3V_{ac}$  bias): (a) to (c) are the amplitude images obtained from the 1st, 2nd and 5th BE-ESM imaging, respectively; (d) to (f) are calculated diffusion coefficient maps, respectively; and (g) average diffusion coefficient vs. the number of BE-ESM images, and the error bars indicate the variation of the diffusion coefficient within the image. The BE-ESM images are obtained with a pixel density of  $64 \times 64$  over  $1 \times 1 \mu\text{m}^2$ .



number of factors: (i) the Li-ion concentration difference existing in different regions, higher electrochemical strain (larger deformation) represents higher Li-ion concentration; (ii) the heterogeneity and anisotropy of the sample surface caused by different grain structures. Li-ions are relatively easier to diffuse along preferred directions; as a result, Li-ion movement within the material is anisotropic; and (iii) the different crystallographic orientations of the grains under bias. For an actuated grain with *c*-axis aligned normally to the substrate, the detected deformation (or strain) is maximal because small amounts of Li-ion concentration variation can induce a large amount of *c*-axis fluctuation.<sup>34</sup> However, this factor may be eliminated in this study as most of grains in the Li-rich cathode film are (003) oriented.

Fig. 3(c) and (d) show that after 2nd to 5th BE-ESM imaging, the grain size and morphology are fairly similar to those after the 1st BE-ESM imaging. From the line profile analysis [Fig. 3(i)], the height remains almost the same in the 2nd to 5th BE-ESM images. This suggests that the movement of certain Li-ions during 1st BE-ESM imaging may be irreversible, as these Li-ions cannot return to their previous positions after 1st BE-ESM imaging. On the other hand, Fig. 4(b) and (c) still show non-zero electrochemical strain. This indicates that certain bias-induced Li-ion movement still occurs during 2nd to 5th BE-ESM imaging. However, the movement of these Li-ions does not cause significant changes in the topographic image, suggesting reversible Li-ion movement. Hence, the bias-induced Li-ion redistribution is partially reversible in the Li-rich cathode film after the 1st BE-ESM image. Generally speaking, the strengths of the electrochemical strain from 1st to 5th BE-ESM images continually decrease [Fig. 4(a) to (c)]. The ESM amplitudes approximately approach to a value of  $\sim 0.48$  pm; this indicates there may be a concentration limit for reversibly movable Li-ions. Since BE-ESM is conducted at a high frequency regime, the dependence of electrochemical strain on the region of the tip-surface contact is generally weak.<sup>16</sup> Therefore, the reduced amplitude response reveals that under repeated electric field, the electrochemical activity of Li-ions gradually attenuates.

Fig. 4(d) to (f) are 3D spatial maps of the calculated local diffusion coefficients (overlaid on topographic images) during the multiple BE-ESM imaging. As the number of the BE-ESM images increases, the diffusion coefficient reduces significantly. From the 1st to 5th BE-ESM images, the regions with higher diffusion coefficients (purple and green colour regions) reduce and the regions with lower diffusion coefficients (red and yellow colour regions) increase. The averaged diffusion coefficient across the imaged area can be extracted and fitted on a Gaussian-type plot. Fig. 4(g) shows the average diffusion coefficient and the standard deviation as a function of the numbers of the BE-ESM image. The local diffusion coefficients decrease continuously with the increase in number of BE-ESM images. In addition, the variation in the diffusion coefficient within one image is also reduced. The reasons for this are most likely the permanent trapping of Li-ions in grain structures, as well as the electrochemical fatigue and degradation under repeated electric field. Furthermore, the decrease of the local diffusivity value is more significant after the 1st imaging with the initial local diffusivity decreases by  $\sim 45\%$ , which is approximately

60% of the total loss of the local diffusivity in the material. From the perspective of battery cycling performance, the observed irreversible topography change and the diffusivity loss at the nanoscale can be correlated with each other to study the capacity loss of the Li-rich cathode materials at the device level.

### *In situ* relaxation mapping due to diffusion

Fig. 5(a) and (b) show the AFM deflection image on an area of  $1 \times 1 \mu\text{m}^2$  of Li-rich thin film cathode before and after BE-ESM

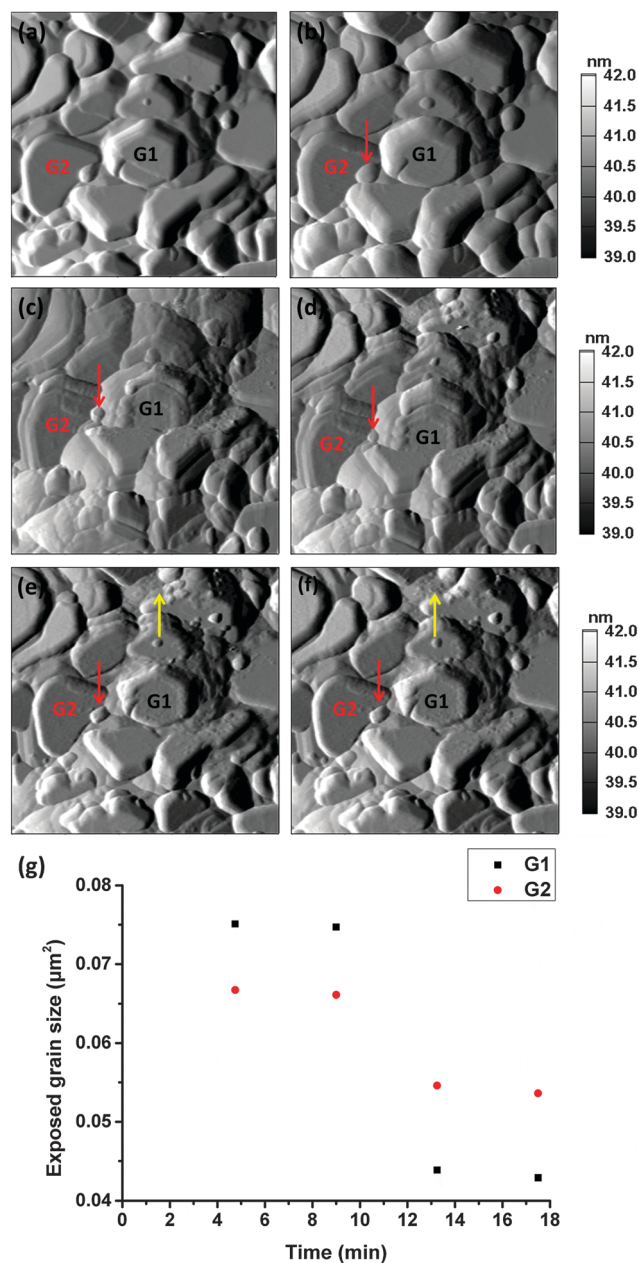


Fig. 5 (a) and (b) are the AFM deflection images on an area of  $1 \times 1 \mu\text{m}^2$  of the Li-rich thin film cathode before and after BE-ESM measurement with  $3V_{ac}$ ; (c) to (f) are four continuous AFM deflection images scanned immediately after a BE-ESM measurement with  $4V_{ac}$ ; (g) grain size evolution as a function of time. All the AFM images were scanned by a pixel density of  $256 \times 256$  and a scan rate of 1 Hz.





measurement with  $3V_{ac}$ . As the actuated grain is saturated with lithium, it is found that a higher bias is required to overcome the necessary chemical potential barrier to intercalate more Li-ions into the cathode layers.<sup>34</sup> Therefore, the BE-ESM image with  $4V_{ac}$  is conducted on the same area, after which a series of continuous AFM scans (only the first four are shown here) are immediately conducted. The corresponding AFM images are shown in Fig. 5(c) to (f). After BE-ESM with a higher bias, most grains show a greater degree of expansion than that with  $3V_{ac}$ , as illustrated by grain G1 and G2 in Fig. 5(b) and (c). The extent of Li-ion movement within the thin film depends on the applied cyclic voltage. Higher voltage can cause larger changes in the Li-ion concentration under the SPM tip, resulting in more dramatic volumetric changes. Certain grains (marked by red arrow) show a slight decrease in the grain size. An interesting observation is that, during the third AFM image, grain contraction is observed, as illustrated by G1 and G2 in Fig. 5(e). At the same time, the grain marked by the red arrow expands slightly. The fourth scan shows only a little topography changes, as marked by a yellow arrow in Fig. 5(f). The topography remains the same after the fourth scan. The topography changes from Fig. 5(c) to (f) indicate a redistribution of Li-ions without the presence of an electric field. In addition, the time consumed for mode switching (from BE-ESM to AFM) and parameter adjustment is approximately 30 seconds. The time consumed for each AFM scan is about 4 minutes and 15 seconds. As shown in Fig. 5(g), the grain sizes of both grains (G1 and G2) decrease significantly with time, especially after 9 minutes. Here, the observed topography changes as time elapse (relaxation) is attributed to Li-ion diffusion. It should be noted that the degree of topography changes and relaxation time depend on the specific grain configuration and connectivity of the grain junction. The shrinkage of a grain (*a*-axis contraction) indicates a decrease in the amount of Li-ions in this individual grain, *i.e.*, Li-ions are extracted out of this grain. If a grain is over-saturated with Li-ions, then a certain amount of Li-ions can release out to maintain stability of the grain structure, and this results in grain shrinkage. For the thin film cathode used here, the grains are connected and piled up layer by layer. However, the evolution of the lattice parameter due to the Li-ion intercalation/de-intercalation of the Li-rich cathode cannot be determined under current conditions. Therefore, it is not possible, at least for now, to quantify the exact amount of Li-ions inserting/extracting through grains from the information obtained by AFM images alone.

## Conclusions

In summary, this paper has presented the results of *in situ* studies on Li-ion diffusion at the nanoscale in Li-rich layered oxide cathode film using SPM techniques (BE-ESM and AFM). The results show that the local diffusion coefficients can be mapped from the ESM images. The topography changes due to Li-ion diffusion are observed and bias-induced Li-ion redistribution is partially reversible. Li-ion diffusivity attenuates gradually over several BE-ESM images and the loss is mainly during the

first imaging. Furthermore, topography evolution as a function of time (relaxation) is observed. In addition, this work shows that the BE-ESM technique provides a powerful approach to induce the localized Li-ion movement at nano- to micro-scales. The results also demonstrate that by combining the AFM topography images with the electrochemical deformation from the BE-ESM images, the Li-ion diffusion behaviour can be studied. However, one of the limitations of the SPM technique is the lack of the chemical information on the materials, hence limiting the detailed physical chemistry oriented interpretations and visualization of Li-ion diffusion processes in the materials. However, the SPM technique can be used to detect the changes in the localized properties. In this sense, this method and analysis are suitable to study the changes in the various properties that the cathode materials undergo during the charge/discharge processes. In addition, this work also offers a fundamental understanding of the ion diffusion phenomena and underlying mechanisms in the cathode material under the electric field. In addition, this work also shows the significance of the SPM-based techniques to the Li-ion battery research; and the measurements developed in this research can also be extended to other oxide materials.

## Acknowledgements

This work is supported by Ministry of Education (Singapore) through the National University of Singapore under Academic Research Fund (R-265-000-406-112). One of the author (YS) would also like to thank the support of scholarship by the Ministry of Education (Singapore) under the Academic Research Fund (R-265-100-406-112).

## References

- 1 A. Manthiram, *J. Phys. Chem. Lett.*, 2011, **2**, 176–184.
- 2 B. Scrosati and J. Garche, *J. Power Sources*, 2010, **195**, 2419–2430.
- 3 J. M. Clark, S. Nishimura, A. Yamada and M. S. Islam, *Angew. Chem., Int. Ed.*, 2012, **51**, 13149–13153.
- 4 J. W. Fergus, *J. Power Sources*, 2010, **195**, 939–954.
- 5 H. J. Yu and H. S. Zhou, *J. Phys. Chem. Lett.*, 2013, **4**, 1268–1280.
- 6 L. Li, K. S. Lee and L. Lu, *Funct. Mater. Lett.*, 2014, **07**, 1430002.
- 7 Y. Wu and A. Manthiram, *Electrochem. Solid-State Lett.*, 2006, **9**, A221–A224.
- 8 W. C. West, J. Soler, M. C. Smart, B. V. Ratnakumar, S. Firdosy, V. Ravi, M. S. Anderson, J. Hrbacek, E. S. Lee and A. Manthiram, *J. Electrochem. Soc.*, 2011, **158**, A883–A889.
- 9 H. Koga, L. Croguennec, P. Mannezzies, M. Ménétrier, F. Weill, L. Bourgeois, M. Duttine, E. Suard and C. Delmas, *J. Phys. Chem. C*, 2012, **116**, 13497–13506.
- 10 S. H. Kang, P. Kempgens, S. Greenbaum, A. J. Kropf, K. Amine and M. M. Thackeray, *J. Mater. Chem.*, 2007, **17**, 2069–2077.
- 11 J. Zhu, J. Feng, L. Lu and K. Zeng, *J. Power Sources*, 2012, **197**, 224–230.



- 12 J. Zhu, K. Zeng and L. Lu, *J. Appl. Phys.*, 2012, **111**, 063723.
- 13 X. J. Zhu, C. S. Ong, X. X. Xu, B. L. Hu, J. Shang, H. L. Yang, S. Katlakunta, Y. W. Liu, X. X. Chen, L. Pan, J. Ding and R. W. Li, *Sci. Rep.*, 2013, **3**, 1084.
- 14 N. Balke, S. Jesse, A. N. Morozovska, E. Eliseev, D. W. Chung, Y. Kim, L. Adameczyk, R. E. Garcia, N. Dudney and S. V. Kalinin, *Nat. Nanotechnol.*, 2010, **5**, 749–754.
- 15 N. Balke, S. Jesse, Y. Kim, L. Adameczyk, A. Tselev, I. N. Ivanov, N. J. Dudney and S. V. Kalinin, *Nano Lett.*, 2010, **10**, 3420–3425.
- 16 A. N. Morozovska, E. A. Eliseev, N. Balke and S. V. Kalinin, *J. Appl. Phys.*, 2010, **108**, 053712.
- 17 S. Jesse, N. Balke, E. Eliseev, A. Tselev, N. J. Dudney, A. N. Morozovska and S. V. Kalinin, *ACS Nano*, 2011, **5**, 9682–9695.
- 18 S. Jesse, A. Kumar, T. M. Arruda, Y. Kim, S. V. Kalinin and F. Ciucci, *MRS Bull.*, 2012, **37**, 651–658.
- 19 N. Balke, E. A. Eliseev, S. Jesse, S. Kalnaus, C. Daniel, N. J. Dudney, A. N. Morozovska and S. V. Kalinin, *J. Appl. Phys.*, 2012, **112**, 052020.
- 20 Q. N. Chen, Y. Y. Liu, Y. M. Liu, S. H. Xie, G. Z. Cao and J. Y. Li, *Appl. Phys. Lett.*, 2012, **101**, 063901.
- 21 J. Zhu, L. Lu and K. Zeng, *ACS Nano*, 2013, **7**, 1666–1675.
- 22 S. Jesse and S. V. Kalinin, *J. Phys. D: Appl. Phys.*, 2011, **44**, 464006.
- 23 S. Jesse, S. V. Kalinin, R. Proksch, A. P. Baddorf and B. J. Rodriguez, *Nanotechnology*, 2007, **18**, 435503.
- 24 M. P. Nikiforov, S. Jesse, A. N. Morozovska, E. A. Eliseev, L. T. Germinario and S. V. Kalinin, *Nanotechnology*, 2009, **20**, 395709.
- 25 B. Yan, J. Liu, B. Song, P. Xiao and L. Lu, *Sci. Rep.*, 2013, **3**, 3332.
- 26 J. B. Bates, N. J. Dudney, B. J. Neudecker, F. X. Hart, H. P. Jun and S. A. Hackney, *J. Electrochem. Soc.*, 2000, **147**, 59–70.
- 27 H. Xia and L. Lu, *Electrochim. Acta*, 2007, **52**, 7014–7021.
- 28 H. Katsui, Y. Yamashita, R. Tu and T. Goto, *J. Ceram. Soc. Jpn.*, 2013, **121**, 406–410.
- 29 P. J. Bouwman, B. A. Boukamp, H. J. M. Bouwmeester and P. H. L. Notten, *J. Electrochem. Soc.*, 2002, **149**, A699–A709.
- 30 P. J. Bouwman, B. A. Boukamp, H. J. M. Bouwmeester, H. J. Wondergem and P. H. L. Notten, *J. Electrochem. Soc.*, 2001, **148**, A311–A317.
- 31 A. Suzuki and Y. Mishin, *J. Mater. Sci.*, 2005, **40**, 3155–3161.
- 32 N. Balke, S. Kalnaus, N. J. Dudney, C. Daniel, S. Jesse and S. V. Kalinin, *Nano Lett.*, 2012, **12**, 3399–3403.
- 33 A. Cléménçon, A. T. Appapillai, S. Kumar and Y. Shao-Horn, *Electrochim. Acta*, 2007, **52**, 4572–4580.
- 34 D. Chung, N. Balke, S. V. Kalinin and R. E. Garcia, *J. Electrochem. Soc.*, 2011, **158**, A1083–A1089.

